

Scattering and absorption imaging of a highly fractured fluid-filled seismogenetic volume in a region of slow deformation

Ferdinando Napolitano^a, Luca De Siena^{b,c}, Anna Gervasi^{d,e}, Ignazio Guerra^d, Roberto Scarpa^a, Mario La Rocca^d

^a*Dipartimento di Fisica "E.R. Caianiello", Università degli Studi di Salerno, Via Giovanni Paolo II, 84084, Fisciano (SA), Italy. **email to:** fnapolitano@unisa.it*

^b*Institute of Geosciences, Johannes Gutenberg University Mainz, J.-J.-Becher-Weg 21, D-55128 Mainz, Germany*

^c*University of Aberdeen, School of Geosciences, Geology and Petroleum Geology, Meston Building, King's College, Aberdeen AB24 3UE Scotland, UK*

^d*Dipartimento di Biologia, Ecologia e Scienze della Terra, Università della Calabria, Ponte P. Bucci, 87036, Arcavacata di Rende (CS), Italy*

^e*Istituto Nazionale di Geofisica e Vulcanologia, Sezione di Rende (CS), Ponte P. Bucci, 87036, Arcavacata di Rende (CS), Italy*

Abstract

Regions of slow strain often produce swarm-like sequences, characterized by the lack of a clear mainshock-aftershock pattern. The comprehension of their underlying physical mechanisms is challenging and still debated. We used seismic recordings from the last Pollino swarm (2010-14) and nearby to separate and map seismic scattering (from P peak-delays) and absorption (from late-time coda-wave attenuation) at different frequencies in the Pollino range and surroundings. High-scattering and high-absorption anomalies are markers of a fluid-filled fracture volume extending from SE to NW (1.5-6 Hz) across the range. With increasing frequency, these anomalies approximately cover the area where the strongest earthquakes occurred from the sixteenth century until 1998. In our interpretation, the NW fracture propagation ends

where carbonates of the Lucanian Apennines begin, as marked by a high-scattering and low-absorption area. At the highest frequency (12 Hz) the anomalies widen southward in the middle of the range, consistently marking the faults active during the recent Pollino swarm. Our results suggest that fracture healing has closed small-scale fractures across the SE faults that were active in the past centuries, and that the propagation of fluids may have played a crucial role in triggering the 2010-2014 Pollino swarm. Assuming that the fluid propagation ended at the carbonates barrier in the NW direction, fractures opened new paths to the South, favoring the nucleation of the last Pollino swarm. Indeed, the recently active faults in the middle of the seismogenic volume are marked by a high-scattering and high-absorption footprints. Our work provides evidence that attenuation parameters may track shape and dynamics of fluid-filled fracture networks in fault areas.

Keywords: Pollino, seismic attenuation, scattering, fluids, fractures, healing.

1. Introduction

The southern Apennines and the Calabrian arc are among the most seismically-active areas of the Mediterranean region. Despite the intense seismic activity, gaps in historical documentation (Scionti et al., 2006) and the low population density of the area (Cinti et al., 1997) have marked the Pollino range as a "seismic gap" between the southern Apennine and the Crati Valley (Rovida et al., 2011; Tertulliani and Cucci, 2014) (Figure 1). Paleoseismological investigations show clear evidence of large-magnitude earthquakes (M6.5-7) occurred along two seismogenic areas, the Pollino and

10 Castrovillari faults (POL and CAS in Figure 1) (Cinti et al., 1997, 2002). A
11 few earthquakes of moderate magnitude occurred during seismic sequences
12 struck these areas in the past centuries, as the 1693 Pollino seismic sequence
13 (Tertulliani and Cucci, 2014) or the 1708 earthquake ($M_L 5.5$). In 1998, a
14 $m_L = 5.0$ earthquake occurred in the Mercure basin, northwest of the Pollino
15 massif, triggering the Pollino-Mercure basin sequence (Guerra et al., 2005).
16 Although the uncertainties on the location of historical events are higher
17 than for recent seismicity, there is evidence of a migration of the seismogenic
18 volumes from SE to NW across the Pollino range between 1559 and 2014
19 (Figure 1). Between 2010 and 2014 a sequence of almost 10.000 earthquakes
20 of small-to-moderate magnitude with two mainshocks of $M_L 4.3$ and $M_L 5.0$
21 occurred in the Pollino area (Totaro et al., 2015; Passarelli et al., 2015) (Fig-
22 ures 1-2). During this sequence, characterized by a migration in time from
23 NW toward SE (Fig. 1), a slow-slip event lasting several months (between
24 2012 and 2013) was detected in the same area via the GPS monitoring net-
25 work (Cheloni et al., 2017). Seismic data have been used in combination
26 with geological and remote-sensing data to map seismically-active normal
27 faults Brozzetti et al. (2017) and to evaluate local site effects (Napolitano
28 et al., 2018) in the area. The relationship between slow-strain areas, often
29 characterized by a combination of seismic brittle failures and aseismic slip,
30 and swarm-like seismic activity is one of the possible scenarios proposed, e.g.,
31 by Lohman and McGuire (2007); Peng and Gombert (2010); Passarelli et al.
32 (2015). Even though the correlation between swarm-like activity and their
33 fault mechanisms is not fully understood, these works suggest that aseismic
34 processes are a general and common feature driving swarm-like sequences.

35 For this reason, novel geophysical imaging is necessary to improve hazard
36 estimation for earthquakes that, in slow-strain regions, are episodic and spa-
37 tially migrating (Landgraf et al., 2017).

38 Seismic attenuation tomography has the potential to image the extension
39 of highly-fractured volumes, especially when fluids saturate them inducing
40 seismicity (De Siena et al., 2016, 2017; Amoroso et al., 2017). The two
41 physical mechanisms that induce inelastic attenuation while a wave travels
42 through the crust are seismic scattering and absorption. The introduction of
43 the radiative transfer equation solved by numerical Monte Carlo simulations
44 put forward the important role of multiple scattering in the generation of coda
45 waves (Paasschens, 1997; Sato et al., 2012). In their seminal paper, Gusev
46 and Abubakirov (1999) devise a strategy to invert the broadening envelopes
47 (the seismic intensities recorded at a station, Fig. 3) for transport turbidity,
48 a single parameter describing scattering attenuation and back-scattering of
49 coda waves. At crustal scale, the peak-delay time (i.e. the time lag from
50 the direct-wave onset to the maximum amplitude of the signal envelope) is
51 generally considered a direct measure of multiple forward scattering after
52 correcting for path-propagation (Saito et al., 2002; Takahashi et al., 2007;
53 Calvet and Margerin, 2013).

54 Coda waves (the later portion of the seismogram) are the main manifes-
55 tation of the redistribution of seismic energy caused by multiple scattering.
56 Their attenuation (Q_c^{-1}) is measured from the exponential decay of coda
57 energy envelopes with time (Aki and Chouet, 1975). At long lapse times
58 and in a uniform anisotropic half-space, coda waves theoretically enter the
59 diffusive regime, which in turn implies equality between coda attenuation

60 and absorption (Shapiro et al., 2000). This assumption is valid at regional
61 scale for seismicity constrained in the crust, i.e. in a thick layer regime (Calvet
62 et al., 2013; Margerin, 2017) - which in turn means that earthquakes
63 are mostly constrained inside a thick ($\leq 30km$) crust. At late lapse times,
64 coda waves from these earthquakes have undergone multiple scattering in-
65 teractions: equipartition between P- and S-waves (Hennino et al., 2001) is
66 considered a good marker of the diffusion regime in this setting. Calvet and
67 Margerin (2013) demonstrate that coda-wave attenuation at $t_W = 80$ s is a
68 measurement of seismic absorption for epicentral distances between 0 and 90
69 km in the Pyrenees. Borleanu et al. (2017) use a similar assumption to im-
70 age Vrancea (Romania), revealing extension and shape of sedimentary basins.
71 The joint use of peak-delays and Q_c^{-1} in a thick crust like the Pollino area
72 (average Moho depth at 45km) thus allows to separate scattering attenuation
73 from absorption.

74 Q_c^{-1} regionalisation can reconstruct the geotectonic characteristics of seis-
75 mogenic regions (eg Ugalde et al., 2002). Nevertheless, while peak-delays are
76 sensitive to a tight area around the seismic rays (Saito et al., 2002), assign-
77 ing Q_c^{-1} to ray paths between source and receiver is inaccurate (Del Pezzo
78 et al., 2016). Also, the regionalisation approach hinders testing of anomalies
79 as it does not use a proper forward model for inversion. Recently, modelling
80 of coda amplitude through kernel functions has been proposed (Margerin
81 et al., 2015; Del Pezzo et al., 2016) and tested (Mayor et al., 2016; De Siena
82 et al., 2017) at crustal and local (volcanic) scales. Most of these functions are
83 computed via a Monte Carlo numerical simulation of the Energy Transport
84 Equation. With the above-mentioned assumptions, the multiple anisotropic

85 scattering process leads to diffusion in a time-window where equipartition
86 takes place (Hennino et al., 2001; Souriau et al., 2011) and in the absence
87 of leakage and strong boundary conditions (De Siena et al., 2013; Margerin,
88 2017). All studies agree that in this case the functions have two maxima
89 at source and station positions and expand around them depending on the
90 average scattering properties of the medium (eg Obermann et al., 2013; Del
91 Pezzo et al., 2016).

92 We used earthquakes of the 2010-2014 Pollino sequence and crustal earth-
93 quakes recorded in the surrounding area [lon: 15.4, 16.4; lat: 39.6, 40.4] to
94 produce 2D maps showing the spatial variations of peak-delay time and Q_c^{-1} .
95 While we regionalized peak-delay measurements, we used an analytic ap-
96 proximation of the diffusive sensitivity kernels (Del Pezzo et al., 2016) to
97 model the effective amplitude decrease of coda waves at late lapse times,
98 and inverted Q_c^{-1} in space (De Siena et al., 2017). We tested the resolution
99 and reliability of the final results by inverting on grids having different steps,
100 changing damping parameters and performing checkerboard tests. We use
101 these maps as a proxy of the lateral variations of seismic scattering and ab-
102 sorption in the Pollino area, allowing us to image fault structures, fracture
103 networks, and their influence on fluid propagation and seismicity between
104 the 16th century and today.

105 **2. Geological and geophysical settings**

106 The Pollino area (Southern Italy) is a transition zone between the South-
107 ern Apennines NE-verging collision and the Calabrian rollback subduction
108 zone. Located on the northern side of the Calabrian fore-arc and accretionary

109 wedge, it is a striking example of the faster subduction (relative to the normal
110 subduction in the Mediterranean) of the African under the European plate
111 (Faccenna et al., 1996). The Calabrian fore-arc collided with the continen-
112 tal margins of Nubia, forming the Maghrebides, and of Apulia, forming the
113 Apennines. Two shallow tectonic units coexist in the Pollino transition zone:
114 1) the allochthonous *Liguride Unit*, representing the remnants of the northern
115 continental margin of Neotethys (Cello et al., 1996) and 2) the *Apennines*
116 *Platform*, a thick carbonate shelf succession represented by the Verbicaro
117 Unit overlaying the Pollino Unit. Furthermore, in the Campotenese area,
118 the superposition of the Verbicaro unit onto the Campotenese-Pollino unit
119 is marked by a ductile shear zone along which the Jurassic-lower Miocene
120 carbonate sequence of the Pollino unit is strongly deformed.

121 In this complex geological setting, medium to strong earthquakes ($4 \leq$
122 $M \leq 6$) occur on the northwest flank of the Pollino Range and Mercure
123 basin area on roughly SE-NW trending normal faults (Brozzetti et al., 2017).
124 The earthquakes accommodate the arc-normal northeast-southwest exten-
125 sion. Left lateral strike-slip regional faults oriented WNW-ESE (Van Dijk
126 et al., 2000) and alignments of East- and West-dipping normal faults have
127 been found in the area. Meanwhile, on the Tyrrhenian coastal side, regional
128 East-dipping normal faults have been recognized across north Calabria.

129 Figure 1 shows a map of a wide area including the Pollino Range and its
130 surroundings. Here, we show the known faults taken from both the detailed
131 mapping of Brozzetti et al. (2017) for the Pollino range, and ITHACA cata-
132 logue for the outermost main structures, as well as other geological features
133 considered in the interpretation. The same figure shows the epicenters of

134 monitored (yellow) and historical (orange) earthquakes occurred in the area
135 (taken from Ferranti et al. (2017)), and the epicentral area of the last seismic
136 sequence (2010 – 2014, red ellipse). The locations of historical earthquakes
137 are achieved using the Boxer method (Gasperini et al., 2010) based on the
138 evaluation of the epicenter as the center of mass of largest intensities. Even if
139 this methodology was tested using more recent epicenters, the uncertainties
140 that afflict these locations are much higher than those of monitored events,
141 in the order of some km. Nevertheless, taken into account the location errors,
142 epicenters follow an SE-to-NW trend through time, at least until the 1998
143 Mercure basin earthquake.

144 **3. Data and methods**

145 We have analyzed velocity waveforms data recorded by permanent and
146 temporary seismic stations operating in the Pollino area during the 2010 –
147 2014 seismic sequence. We selected 117 crustal earthquakes of local magni-
148 tude (M_L) ranging from 1.8 to 4.3, source-receiver distance between 1 and 72
149 km, and depths between 2 and 56 km. We performed the waveform selection
150 to obtain a satisfactory coverage of crossing rays across the area. However,
151 while hundreds of events were available in the central part, most of them
152 being located roughly in the same spot, fewer were found in other volumes
153 around the 2010-2014 sequence. Most of the selected events ($\sim 80\%$) are
154 located at depth smaller than 10 km (Supplementary materials, Figure S1).
155 To increase the ray coverage filling gaps were left by shallower we used deeper
156 crustal earthquakes; nevertheless, only 7 of them ($< 2\%$) are deeper than 30
157 km.

158 Since the seismic sequence continued for years at a variable rate, the
159 number of temporary stations often changed in the area. The selected data
160 set includes 21 seismic stations, some of which were permanent while others
161 were operated from months to some years by three institutions: 1) *Università*
162 *della Calabria*; 2) *Istituto Nazionale di Geofisica e Vulcanologia (INGV)*; 3)
163 *GFZ* (Figure 2). Data of INGV and GFZ stations were downloaded from
164 the EIDA online database (Bianchi et al., 2015). The distribution of seismic
165 stations and earthquakes is crucial to test the reliability of our results. Since
166 we used data coming from three different databases, the selected earthquakes
167 were located before any other analysis.

168 We selected 911 waveforms with clear P-wave phase and coda-to-noise
169 ratio higher than 3 at 30 s from the origin time in the frequency range 1 Hz
170 - 32 Hz. The final dataset also comprises 357 waveforms with clear picking
171 of both P and S waves, the first used for pick-delay mapping. We bandpass-
172 filtered the whole seismograms in 5 frequency bands (1-2 Hz, 2-4 Hz, 4-8
173 Hz, 8-16 Hz, 16-32 Hz) applying a Butterworth filter of order 4, forward and
174 backwards. We computed envelopes from the absolute value of the Hilbert
175 transform of the signal. We then smoothed them with a moving window of
176 length 8 times the inverse central frequency - an average between what is
177 used between regional (Calvet and Margerin, 2013) and local volcanic (De
178 Siena et al., 2016) scales.

179 *3.1. Peak-delay time measurement and mapping*

180 We measure the peak-delay time as the lag between the P-wave onset
181 and the maximum S wave amplitude (Takahashi et al., 2007). The base-10
182 logarithm of the peak-delay time ($t_r^T(f)$, in seconds) is related to the base-10

183 logarithm of the epicentral distance (R , in km) in each frequency band f by:

$$\log_{10}(t_r^T(f)) = A_r(f) + B_r(f)\log_{10}(R) \quad (1)$$

184 where A_r and B_r are the coefficients of the fit (Figure S2 in supplementary
 185 material). The variations of the peak-delay time with respect to these trends
 186 ($\Delta\log_{10}(t_r(f))$):

$$\Delta\log_{10}(t_r(f)) = \log_{10}(t_r(f)) - \log_{10}(t_r^T(f)) \quad (2)$$

187 do not depend on geometrical propagation. They are assumed as a measure
 188 of the relative strength of accumulated S wave scattering along each ray path
 189 (Saito et al., 2002). In other words, high values of $\Delta\log_{10}(t_r(f))$ mean that
 190 the ray path crosses regions of high heterogeneity (Calvet et al., 2013). For
 191 the mapping, we selected the area shown in Figures 1 and 2 (lon: 15.4, 16.4;
 192 lat: 39.6, 40.4) and divided it into rectangular blocks of size $0.05^\circ \times 0.05^\circ$.
 193 We thus evaluated peak-delays along 2D source-receiver rays and assigned
 194 their values to each node with a regionalisation approach (Takahashi et al.,
 195 2007) (Figure 4). Even though no exact forward model exists, we tested the
 196 stability of the results by repeating the same analysis in a rectangular grid
 197 of steps $0.1^\circ \times 0.1^\circ$ (Figure S2). We then interpreted only patterns recovered
 198 by the test and where Q_c^{-1} is recovered by resolution tests (see next section).

199 3.2. Inverse coda- Q measurement and mapping

200 We consider the energy envelope decay of coda waves described by Aki
 201 and Chouet (1975) using the following equation:

$$E(t, f) = S(f)t^{-\alpha} \exp\left(\frac{-2\pi ft}{Q_C}\right) \quad (3)$$

202 where $E(t, f)$ is the power spectral density, $S(f)$ is a source/site term, t is
 203 the lapse-time from the origin of the event, and $Q_c^{-1}(f)$ is the frequency-
 204 dependent inverse coda quality factor. α is equal to $3/2$ in a layer character-
 205 ized by an anisotropic multiple scattering regime (Paasschens, 1997; Calvet
 206 et al., 2013). The choice of the coda window is crucial to map stable lateral
 207 variations of seismic attenuation. We want to exclude the increasing tran-
 208 sient regime occurring at short lapse time as shown by Calvet and Margerin
 209 (2013) while we require a signal-to-noise ratio greater than 5 across the whole
 210 window of analysis. Coda windows in our work start at lapse time $t_W = 15s$
 211 from the origin-time of the selected earthquake and are characterized by a
 212 length of $L_W = 10s$ (Figure 3). This coda window provides envelopes with
 213 sufficient energy for measuring Q_c^{-1} at four of the five previously-mentioned
 214 frequency bands (Figure 5). At 18 Hz, a significant number of envelopes
 215 present a signal-to-noise ratio lower than 5; we considered the results at this
 216 frequency as unreliable and analyzed only the remaining frequencies.

217 In our time window, equipartition is achieved after 15 seconds (red line
 218 in figure 5) while Q_c^{-1} shows no consistent variations with epicentral distance
 219 (Supplementary Materials, figure S3). In the absence of leakage (Calvet and
 220 Margerin, 2013; Margerin, 2017) we can thus interpret Q_c^{-1} as a measurement
 221 of absorption. Still, we need to acknowledge the effect of leakage on our
 222 data. Our scale is similar to that of Gaebler et al. (2015) (0.5×0.5 degrees
 223 squared), who estimate a transport mean free path of $l=50-110$ km between
 224 3 and 24 Hz, approximately our frequency range. The ratio between the
 225 transport mean free path and the average crustal thickness $H=45$ km (Piana
 226 Agostinetti and Amato, 2009) thus varies between $H=0.4$ and $H=1$. The

227 effect of leakage is thus not negligible but still well above the limit ($H=0.2$)
 228 where equipartition brakes down (Margerin, 2017).

229 We used a non-linear approach to solve equation 3 in the other four
 230 frequency bands (1 - 2 Hz, 2 - 4 Hz, 4 - 8 Hz, 8 - 16 Hz). We divided the
 231 envelope of seismic coda waves between 15 s and 25 s in windows of length 2s
 232 for each source-station pair. Then, we normalized the energy in each smaller
 233 window dividing by that of the last window to remove the source effect, $S(f)$.
 234 We used a grid search on 1000 trial Q_c values to find the best solution. In each
 235 window, we subtracted the normalized energy and the model, then minimized
 236 the residual L1 norm for all time windows. This non-linear solution is more
 237 stable than the standard linearized technique for coda signals having low
 238 signal-to-noise ratios (Ibanez et al., 1993).

239 We mapped the sensitivity of the Q_c^{-1} parameters to space (x,y) by com-
 240 puting diffusive sensitivity kernels (Del Pezzo et al., 2016) (Figure S4 in
 241 Supplementary Material). For each source – receiver pair of coordinates $(x_s,$
 242 $y_s)$ and (x_r, y_r) , the kernels are defined as follows:

$$\begin{aligned}
 f[x, y, x_r, y_r, x_s, y_s] = & \frac{1}{4\pi\delta_x D^2 \delta_y} \exp \left[-\frac{(x - \frac{x_r+x_s}{2})^2}{2(\delta_x D)^2} + \frac{(y - \frac{y_r+y_s}{2})^2}{0.5(\delta_y D)^2} \right] + \\
 & + \frac{1}{2\pi\delta_x D^2 \delta_y} \exp \left[-\frac{(x - x_s)^2}{2(\delta_x D)^2} + \frac{(y - y_s)^2}{2(\delta_y D)^2} \right] + \\
 & + \frac{1}{2\pi\delta_x D^2 \delta_y} \exp \left[-\frac{(x - x_r)^2}{2(\delta_x D)^2} + \frac{(y - y_r)^2}{2(\delta_y D)^2} \right]
 \end{aligned} \quad (4)$$

243 where δx and δy are the spatial apertures of the weighting functions along
 244 the x and the y axis. These apertures can be set to 0.2 for a wide range of
 245 crustal scattering parameters in a diffusive regime (Del Pezzo et al., 2016).
 246 We set the same area and grid defined for peak-delay analysis, inverting for
 247 the spatial distribution of $Q_c^{-1}(f)$ in space in the four remaining frequency

248 bands (Figure 6). The mapping is performed with the inversion scheme
249 described by De Siena et al. (2017), with the hypothesis that the energy is
250 entirely lost inside the predefined grid. We evaluated effective stability and
251 resolution of the solution by selecting the best damping parameter between
252 the size of the regularized solution and its fit to the given data (L-curves in
253 figure S5). As for peak-delay analysis, we tested the stability of our results
254 with a coarser node spacing (Figure S6). Finally, we tested our resolution
255 performing checkerboard tests with multiple grid node spacing ($0.05^\circ \times 0.05^\circ$
256 grid in figure S7 and $0.1^\circ \times 0.1^\circ$ grid in figure S8).

257 *3.3. Parameter space variation and mapping*

258 We plotted scattering vs absorption measurements in their parameter
259 space after removing the mean computed over all measurements (De Siena
260 et al., 2016). This graphical method makes results clearer on map, relating
261 the relative variation of $Q_c^{-1}(f)$ (horizontal-axis, absorption) to $\Delta \log_{10}(t_r(f))$
262 (vertical-axis, scattering) and setting a color for each possible combination
263 of the space parameter divided in 4 quadrants (Figure S9). In this case, we
264 set: red for high scattering and high absorption (HS-HA), orange for low
265 scattering and high absorption (LS-HA), light blue for high scattering and
266 low absorption (HS-LA), green for low scattering and low absorption (LS-
267 LA). We additionally set gray for values with a level of discrimination less
268 than 1% of the maximum variations. We characterize each node of the grid
269 with the same palette (Figure 7, left column).

270 4. Results

271 Figures 4 and S2 (in Supplementary Materials) show the regionalisation
272 results for peak-delays on 2D map characterized by grids with steps of 0.05°
273 and 0.1° , respectively. Comparison between them shows the stability of pat-
274 terns of dimension equal or greater than $0.1^\circ \times 0.1^\circ$. Figures 6 and S6 (in
275 Supplementary Materials) show the $Q_c^{-1}(f)$ results obtained for the same
276 grid steps. At low frequencies, late coda-to-noise ratios are higher thus pro-
277 viding results affected by lower uncertainties. In a given time window, the
278 coda-to-noise ratio progressively decreases as the frequency increases, thus
279 reducing data used for the analysis at higher frequencies and/or reliability of
280 results. For each frequency band, we computed the L curves (log-log plots
281 of the norm of the regularized solution versus the norm of the correspond-
282 ing residual norm). After testing different damping parameters, we chose
283 0.1 as the best compromise to obtain scattering and absorption maps at all
284 frequencies.

285 4.1. Discussion

286 In Figure 7 we present (left) and interpret (right) the results for each fre-
287 quency band. Due to the depth of the Moho (Piana Agostinetti and Amato,
288 2009), we assume that multiple scattering acts in a anisotropic scattering
289 layer. Most earthquakes are located at depths lower than 10 km, supporting
290 this assumption. The effect of leakage may still be important from previous
291 calculations (Margerin, 2017). Still, the Moho in the study area is mostly flat
292 (Piana Agostinetti and Amato, 2009), minimizing the lateral variations pro-
293 duced by this mechanism. In summary, we can safely assume that our results

294 are representative of the shallow crust and look for any relationships between
295 the observed scattering (peak-delay) and absorption (coda-attenuation) pat-
296 terns and the geological features of the investigated area. We do not ob-
297 serve any orange zone (LS-HA) stable and big enough to be discussed. The
298 Calabro-Lucania coastal range (western side of the maps - Figure 7, left)
299 changes from LS-LA at low frequency (green, 1.5 Hz and 6 Hz) to HS-LA
300 (cyan) at 12 Hz. However, the resolution tests show that the area is unre-
301 solved. The same is true for one of the most stable patterns in frequency,
302 i.e., the green LS-LA zone visible in the north-eastern sector of the maps.

303 A cyan HS-LA pattern both stable in frequency and resolved by our map-
304 ping comprises the part of the Lucanian Apennines (named *LA* in Figure 7,
305 right) extending from Mount Sirino to Lake Pertusillo. Geologically, this
306 is a compact carbonate stand-alone block, surrounded by faults and isolated
307 through clay formations. Fractured volumes of minor importance are present
308 in this block due to the high-compression regime in the region. This geologi-
309 cal configuration likely explains the high scattering values at all frequencies.
310 The low-absorption values are instead a consequence of the cohesion of the
311 carbonate block, which acts as a shield between the extensive northern hy-
312 drocarbon deposit in the Val D’Agri zone and the southern Pollino area.

313 The red-coloured HS-HA patterns are the most remarkable and well-
314 resolved of our study, and the most interesting for an interpretation in terms
315 of fluid-filled fracture networks (Quintal et al., 2014). The faults located in-
316 side it are colored red in the maps on the right side of Figure 7. The Mercure
317 and the Castrovillari basins (MB and CB, respectively) are both character-
318 ized by shallow-marine deposits. The former is filled with alluvial, fluvial-

319 deltaic and lacustrine sediments (Ferranti et al., 2017); the latter is filled with
320 clay, sand (in the shallower layer), fine marine sediments, and conglomerates.
321 Both basins are likely characterized by high absorption, contributing to the
322 red pattern. The HS-HA red pattern marks the fault system underneath the
323 Pollino Range at 6 and 12 Hz. We suggest a relationship with the prominent
324 geological characteristic of a multiple fragmented shallow-water carbonate
325 succession. The Lauria mountains (LM) are the north-west extension of the
326 carbonate succession of the Pollino Ridge, and they are characterized by the
327 same HS-HA (red) at the same frequencies.

328 The HS-HA pattern changes its position with changing frequency. At 1.5
329 Hz, the red area marks the S-SE sector of the map, crossed by extensive fault
330 networks; at 3 Hz the pattern is still present in the SE sector but becomes
331 predominant in the Pollino area. The red color spreads across the Mercure
332 basins and the Lauria mountains at 6 Hz, and fills the area of the 2010-
333 2014 seismic swarm at 12 Hz. The relatively high-absorption values correlate
334 well with the high v_P/v_S values found in the same area by (Barberi et al.,
335 2004, figure 7) and by Totaro et al. (2015). The results confirm the scenario
336 proposed for the 2010-2014 seismic swarm by Passarelli et al. (2015) of a
337 large role played either by the increase of pore pressure or fluid infiltration
338 within the seismogenic zone in favouring the aseismic slip by lowering the
339 normal stress on the fault plane.

340 Historical earthquake locations are affected by significant uncertainties,
341 differently from those occurred in the last 20 years. Even considering these
342 uncertainties, the HS-HA pattern migrates with increasing frequency fol-
343 lowing the chronological order of historical earthquakes from the sixteenth

344 century until Pollino swarm. The most recent earthquakes, e.g., the Mercure
345 basin earthquake and the Pollino swarm itself, likely reactivate small fracture
346 networks as fluids migrate along the main faults, modifying the way fluids
347 permeate fault structures. Poro-elasticity studies proved the central role of
348 fluid pressure diffusion between connected fractures, and showed how the
349 behavior of the connected fracture system is frequency dependent (Quintal
350 et al., 2014).

351 Hunziker et al. (2018) pointed out that the still-unknown relationship
352 between seismic attenuation, diffusion of fluid pressure and fracture connec-
353 tivity can be crucial to identify a highly-fractured volume and track its hy-
354 draulic behavior. Our results strongly suggest such a relationship in some of
355 the fault areas. Changes of peak-delay and Q_c^{-1} with frequency mark in fact
356 heterogeneity of different size (Saito et al., 2002): in the case of faults, small
357 fractured volumes in active zones can only be imaged by shorter-wavelength
358 (higher-frequency) attenuation parameters. While these fracture networks
359 heal quickly, in seismically-active areas they continuously reactivate due to
360 distant seismicity (Xue et al., 2009), at least where fluids are abundant.
361 The healing of smaller fractures is instead permanent in areas not deformed
362 by recent activity. Here, larger unhealed structures should be visible from
363 their long-wavelength (low-frequency) high-scattering and high-absorption
364 signatures. We thus infer that the migration of the HS-HA patterns with
365 increasing frequency shows the effect of fracture healing (Xue et al., 2009).

366 The anomalies effectively track the migration of seismogenic zones since
367 the sixteenth century (Figure 1) by mapping scattering and absorption changes
368 in frequency inside the fracture-network. While we already confirmed the role

369 of fluids in nucleating historical and recent seismicity (Passarelli et al., 2015),
370 our results support the view that the Pollino swarm represents a change in
371 the usual seismicity trend of the area. The stop to the SE-to-NW migration
372 of the HS-HA pattern at 12 Hz is, in our interpretation, due to the barrier
373 represented by the high-scattering compressed carbonates under the Luca-
374 nian Apennines. Since the Pollino swarm, a permanent network has been
375 installed in the area and may provide sufficient data to test our inferences in
376 the presence of renewed seismic activity.

377 5. Conclusions

378 Peak-delay and inverse coda quality factor have been measured together
379 and mapped using a 2D approximation in four frequency bands to image
380 the scattering attenuation and absorption properties of the slowly-deforming
381 Pollino area (Southern Italy). The pattern of anomalies obtained from our
382 analysis shows a correlation with the geological features of the area and with
383 the progressive shift in location of earthquakes. High-scattering and high-
384 absorption anomalies (HS-HA) change their position from inactive faults in
385 the south/southeastern Castrovillari basin (1.5 Hz) to the northwestern Mer-
386 cure Basin and Pollino swarm area (6-12 Hz) across the fault systems (3 Hz).
387 We infer that the Lucanian Apennine compressed carbonates, marked by
388 high-scattering, constitute a barrier for fracture network connectivity and
389 fluid propagation. The two sedimentary basins are characterized by high
390 absorption. However, high-absorption and high-scattering patterns observed
391 at higher frequency likely reveal fluid-filled fractured volumes of shorter di-
392 mension.

393 At low frequency, the patterns map the structures of the fault systems in-
394 active (1.5 Hz) or fractured by seismic sequences dating back to the sixteenth-
395 eighteenth century (3 Hz). Here, shorter fractures are progressively healed,
396 with high scattering and absorption marking extended fault areas perma-
397 nently deformed. At 6 Hz the anomalies characterize the NW branch of the
398 faults, tracking the seismic activity of the last two centuries up to the Mer-
399 cure basin earthquake (1998). The earthquake migration is likely due to the
400 progressive increase of the contribution of small-scale fluid-filled fractures to
401 scattering and absorption. At the highest frequency (12 Hz) the HS-HA area
402 becomes broader and covers the fault system that generated the last Pollino
403 swarm (2010-2014), SW of the Mercure basin. We infer that the fracture
404 propagation trend was blocked NW by the high-scattering Lucanian Apen-
405 nine carbonates. The scattering and absorption picture described by our
406 interpretation provides an independent view on the well-known geological
407 features of the area, the known fault network, and the migration of seismo-
408 genic zones through the last five centuries, focusing on the important role
409 of fluid saturation. Further observations with better distributed earthquakes
410 and seismic stations may give deeper insight into the physics underlying these
411 processes. More efforts are necessary to apply successfully the laboratory re-
412 sults to the Earth crust, that means in our case to measure or estimate the
413 time scale of processes such as fracture healing and fluid migration through-
414 out connected / not connected fracture networks. Still, our work supports
415 the view that attenuation and scattering parameters are able to reconstruct
416 shape and dynamics of fluid-filled fracture networks in fault areas.

6. Acknowledgements

We thank Giuseppe Palladino and professor Robert Butler for sharing their expertise about the geological features of the target area and Roberto Emanuele Rizzo for the relevant suggestions about the dynamics of fluids through fractures. Incisive comments from two anonymous reviewers greatly improved the quality of the paper. The program used to compute the analysis is the MATLAB[®] code *MuRAT*5.3.6.m, available for downloading at:

<https://github.com/ferdinandonapolitano/Attenuation>.

The ITHACA catalogue we use can be found at:

<http://www.isprambiente.gov.it/it/progetti/suolo-e-territorio-1/ithaca-catalogo-delle-faglie-capaci>.

References

Aki, K., Chouet, B., 1975. Origin of coda waves: Source, attenuation, and scattering effects. *Journal of Geophysical Research* 80, 3322–3342. URL: <http://doi.wiley.com/10.1029/JB080i023p03322>, doi:10.1029/JB080i023p03322.

Amoroso, O., Russo, G., De Landro, G., Zollo, A., Garambois, S., Mazzoli, S., Parente, M., Virieux, J., 2017. From velocity and attenuation tomography to rock physical modeling: Inferences on fluid-driven earthquake processes at the Irpinia fault system in southern Italy. *Geophysical Research Letters* 44, 6752–6760. URL: <https://agupubs.onlinelibrary.wiley.com/doi/abs/10.1002/2016GL072346>, doi:10.1002/2016GL072346.

- Barberi, G., Cosentino, M.T., Gervasi, A., Guerra, I., Neri, G., Orecchio, B., 2004. Crustal seismic tomography in the Calabrian Arc region, south Italy. *Physics of the Earth and Planetary Interiors* 147, 297–314. doi:10.1016/j.pepi.2004.04.005.
- Bianchi, M., Evans, P.L., Heinloo, A., Quinteros, J., 2015. WebDC3 Web Interface. URL: <http://geofon.gfz-potsdam.de/software/webdc3>, doi:10.5880/GFZ.2.4/2016.001.
- Borleanu, F., De Siena, L., Thomas, C., Popa, M., Radulian, M., 2017. Seismic scattering and absorption mapping from intermediate-depth earthquakes reveals complex tectonic interactions acting in the Vrancea region and surroundings (Romania). *Tectonophysics* 706-707, 129–142. URL: <http://www.sciencedirect.com/science/article/pii/S0040195117301476>, doi:https://doi.org/10.1016/j.tecto.2017.04.013.
- Brozzetti, F., Cirillo, D., de Nardis, R., Cardinali, M., Lavecchia, G., Orecchio, B., Presti, D., Totaro, C., 2017. Newly identified active faults in the Pollino seismic gap, southern Italy, and their seismotectonic significance. *Journal of Structural Geology* 94, 13–31. URL: <http://dx.doi.org/10.1016/j.jsg.2016.10.005>, doi:10.1016/j.jsg.2016.10.005.
- Calvet, M., Margerin, L., 2013. Lapse-time dependence of coda Q: Anisotropic multiple-scattering models and application to the Pyrenees. *Bulletin of the Seismological Society of America* 103, 1993–2010. doi:10.1785/0120120239.

- Calvet, M., Sylvander, M., Margerin, L., Villaseñor, A., 2013. Spatial variations of seismic attenuation and heterogeneity in the Pyrenees: Coda Q and peak delay time analysis. *Tectonophysics* 608, 428–439. URL: <http://dx.doi.org/10.1016/j.tecto.2013.08.045>, doi:10.1016/j.tecto.2013.08.045.
- Cello, G., Invernizzi, C., Mazzoli, S., 1996. Structural signature of tectonic processes in the Calabrian Arc, southern Italy: Evidence from the oceanic-derived Diamante-Terranova unit. *Tectonics* 15, 187–200. URL: <https://agupubs.onlinelibrary.wiley.com/doi/abs/10.1029/95TC02356>, doi:10.1029/95TC02356.
- Cheloni, D., D'Agostino, N., Selvaggi, G., Avallone, A., Fornaro, G., Giuliani, R., Reale, D., Sansosti, E., Tizzani, P., 2017. Aseismic transient during the 2010-2014 seismic swarm: Evidence for longer recurrence of M 6.5 earthquakes in the Pollino gap (Southern Italy)? *Scientific Reports* 7, 1–10. doi:10.1038/s41598-017-00649-z.
- Cinti, F.R., Cucci, L., Pantosti, D., D'Addezio, G., Meghraoui, M., 1997. A major seismogenic fault in a 'silent area': the Castrovillari fault (southern Apennines, Italy). *Geophysical Journal International* 130, 595–605. doi:10.1111/j.1365-246X.1997.tb01855.x.
- Cinti, F.R., Moro, M., Pantosti, D., Cucci, L., D'Addenzio, G., 2002. New constraints on the seismic history of the Castrovillari fault in the Pollino gap (Calabria, southern Italy). *Journal of Seismology* 6, 199—217.
- De Siena, L., Amoruso, A., Del Pezzo, E., Wakeford, Z., Castellano, M.,

- Crescentini, L., 2017. Space-weighted seismic attenuation mapping of the aseismic source of Campi Flegrei 1983–1984 unrest. *Geophysical Research Letters* 44, 1740–1748. doi:10.1002/2017GL072507.
- De Siena, L., Calvet, M., Watson, K.J., Jonkers, A.R.T., Thomas, C., 2016. Seismic scattering and absorption mapping of debris flows, feeding paths, and tectonic units at Mount St. Helens volcano. *Earth and Planetary Science Letters* 442, 21–31. URL: <http://dx.doi.org/10.1016/j.epsl.2016.02.026>, doi:10.1016/j.epsl.2016.02.026.
- De Siena, L., Del Pezzo, E., Thomas, C., Curtis, A., Margerin, L., 2013. Seismic energy envelopes in volcanic media: In need of boundary conditions. *Geophysical Journal International* 195, 1102–1119. doi:10.1093/gji/ggt273.
- Del Pezzo, E., Ibañez, J., Prudencio, J., Bianco, F., De Siena, L., 2016. Absorption and scattering 2-D volcano images from numerically calculated space-weighting functions. *Geophysical Journal International* 206, 742–756. doi:10.1093/gji/ggw171.
- Faccenna, C., Davy, P., Brun, J.P., Funicello, R., Giardini, D., Mattei, M., Nalpas, T., 1996. The dynamics of back-arc extension: an experimental approach to the opening of the Tyrrhenian Sea. *Geophysical Journal International* 126, 781–795. URL: <https://onlinelibrary.wiley.com/doi/abs/10.1111/j.1365-246X.1996.tb04702.x>, doi:10.1111/j.1365-246X.1996.tb04702.x.
- Ferranti, L., Milano, G., Pierro, M., 2017. Insights on the seismo-

- tectonics of the western part of northern Calabria (southern Italy) by integrated geological and geophysical data: Coexistence of shallow extensional and deep strike-slip kinematics. *Tectonophysics* 721, 372–386. URL: <http://dx.doi.org/10.1016/j.tecto.2017.09.020>, doi:10.1016/j.tecto.2017.09.020.
- Gaebler, P.J., Eulenfeld, T., Wegler, U., 2015. Seismic scattering and absorption parameters in the W-Bohemia / Vogtland region from elastic and acoustic radiative transfer theory , 1471–1481doi:10.1093/gji/ggv393.
- Gasperini, P., Vannucci, G., Tripone, D., Boschi, E., 2010. The Location and Sizing of Historical Earthquakes Using the Attenuation of Macroseismic Intensity with Distance 100, 2035–2066. doi:10.1785/0120090330.
- Guerra, I., Harabaglia, P., Gervasi, A., Rosa, A.B., 2005. The 1998-1999 Pollino (Southern Apennines, Italy) seismic crisis: tomography of a sequence. *Annals of Geophysics* 48. URL: <https://www.annalsofgeophysics.eu/index.php/annals/article/view/3249>, doi:10.4401/ag-3249.
- Gusev, A.A., Abubakirov, I.R., 1999. Vertical profile of effective turbidity reconstructed from broadening of incoherent body-wave pulses — I . General approach and the inversion procedure. *Geophys. J. Int.* 136, 295–308.
- Hennino, R., Trégourès, N., Shapiro, N.M., Margerin, L., Campillo, M., van Tiggelen, B.A., Weaver, R.L., 2001. Observation of equipartition of seismic waves. *Physical Review Letters* 86, 3447–3450. doi:10.1103/PhysRevLett.86.3447.

- Hunziker, J., Favino, M., Caspari, E., Quintal, B., Rubino, J.G., Krause, R., Holliger, K., 2018. Seismic Attenuation and Stiffness Modulus Dispersion in Porous Rocks Containing Stochastic Fracture Networks. *Journal of Geophysical Research: Solid Earth* 123, 125–143. URL: <https://agupubs.onlinelibrary.wiley.com/doi/abs/10.1002/2017JB014566>, doi:10.1002/2017JB014566.
- Ibanez, J.M., Del Pezzo, E., Martini, M., Patanè, D., de Miguel, F., Vidal, F., Morales, J., 1993. Estimates of Coda-Q Using a Non-Linear Regression. *J. Phys. Earth* 41, 203–219.
- Landgraf, A., Kübler, S., Hintersberger, E., Stein, S., 2017. Active tectonics, earthquakes and palaeoseismicity in slowly deforming continents. Geological Society, London, Special Publications 432, 1–12. URL: <https://pubs.geoscienceworld.org/books/book/1937/chapter/107685676/>, doi:10.1144/SP432.13.
- Lohman, R.B., McGuire, J.J., 2007. Earthquake swarms driven by aseismic creep in the Salton Trough, California. *Journal of Geophysical Research: Solid Earth* 112, 1–10. doi:10.1029/2006JB004596.
- Margerin, L., 2017. Breakdown of equipartition in diffuse fields caused by energy leakage. *European Physical Journal: Special Topics* 226, 1353–1370. doi:10.1140/epjst/e2016-60165-6.
- Margerin, L., Planès, T., Mayor, J., Calvet, M., 2015. Sensitivity kernels for coda-wave interferometry and scattering tomography: Theory and numer-

- ical evaluation in two-dimensional anisotropically scattering media. *Geophysical Journal International* 204, 650–666. doi:10.1093/gji/ggv470.
- Margheriti, L., Amato, A., Braun, T., Cecere, G., D’Ambrosio, C., De Gori, P., Delladio, A., Gervasi, A., Govoni, A., Guerra, I., Lucente, F.P., Moretti, M., Selvaggi, G., 2013. Emergenza nell’area del Pollino: le attività della rete sismica mobile. Technical Report.
- Mayor, J., Calvet, M., Margerin, L., Vanderhaeghe, O., Traversa, P., 2016. Crustal structure of the Alps as seen by attenuation tomography. *Earth and Planetary Science Letters* 439, 71–80. URL: <http://dx.doi.org/10.1016/j.epsl.2016.01.025>, doi:10.1016/j.epsl.2016.01.025.
- Napolitano, F., Gervasi, A., La Rocca, M., Guerra, I., Scarpa, R., 2018. Site effects in the pollino region from the HVSR and polarization of seismic noise and earthquakes. *Bulletin of the Seismological Society of America* 108, 309–321. doi:10.1785/0120170197.
- Obermann, A., Planès, T., Larose, E., Campillo, M., 2013. Imaging preruptive and coeruptive structural and mechanical changes of a volcano with ambient seismic noise. *Journal of Geophysical Research: Solid Earth* 118, 6285–6294. doi:10.1002/2013JB010399.
- Paasschens, J., 1997. Solution of the time-dependent Boltzmann equation. *Physical Review E* 56, 1135–1141. doi:10.1103/PhysRevE.56.1135.
- Passarelli, L., Hainzl, S., Cesca, S., Maccaferri, F., Mucciarelli, M., Roessler, D., Corbi, F., Dahm, T., Rivalta, E., 2015. Aseismic transient driving the

- swarm-like seismic sequence in the Pollino range, Southern Italy. *Geophysical Journal International* 201, 1553–1567. doi:10.1093/gji/ggv111.
- Passarelli, L., Roessler, D., Aladino, G., Maccaferri, F., Moretti, M., Lucente, F.P., Braun, T., De Gori, P., Margheriti, L., Woith, H., Sebastian, H., Eleonora, R., Dahm, T., 2012. Pollino Seismic Experiment (2012-2014). Deutsches GeoForschungsZentrum GFZ Other/Seis. doi:10.14470/9N904956.
- Peng, Z., Gomberg, J., 2010. An integrated perspective of the continuum between earthquakes and slow-slip phenomena. *Nature Geoscience* 3, 599–607. URL: <http://dx.doi.org/10.1038/ngeo940>, doi:10.1038/ngeo940.
- Piana Agostinetti, N., Amato, A., 2009. Moho depth and V_p/V_s ratio in peninsular Italy from teleseismic receiver functions. *Journal of Geophysical Research* 114, B06303. URL: <http://doi.wiley.com/10.1029/2008JB005899>, doi:10.1029/2008JB005899.
- Quintal, B., Jänicke, R., Rubino, J.G., Steeb, H., Holliger, K., 2014. Sensitivity of S-wave attenuation to the connectivity of fractures in fluid-saturated rocks. *Geophysics* 79, WB15–WB24. URL: <http://library.seg.org/doi/10.1190/geo2013-0409.1>, doi:10.1190/geo2013-0409.1.
- Rovida, A., Camassi, R., Gasperini, P., Stucchi, M., 2011. CPTI11, the 2011 version of the Parametric Catalogue of Italian Earthquakes URL:

<http://emidius.mi.ingv.it/CPTI>, DOI: 10.6092/INGV.IT-CPTI11,
doi:10.6092/INGV.IT-CPTI11.

- Saito, T., Sato, H., Ohtake, M., 2002. Envelope broadening of spherically outgoing waves in three-dimensional random media having power law spectra. *Journal of Geophysical Research* 107. doi:10.1029/2001JB000264.
- Sato, H., Fehler, M.C., Maeda, T., 2012. *SeismicWave Propagation and Scattering in the Heterogeneous Earth: Second Edition*. Springer, New York, USA.
- Scionti, V., Galli, P., Chiodo, G., 2006. The Calabrian seismicity during the Viceroyalty of Naples: Sources silence or silent sources? the case of the strong 1744 earthquake. *Bollettino di Geofisica Teorica ed Applicata* 47, 53–72. doi:10.1097/01.ALC.0000023988.43694.FE.
- Shapiro, N.M., Campillo, M., Margerin, L., Singh, S.K., Kostoglodov, V., Pacheco, J., 2000. The energy partitioning and the diffusive character of the seismic coda. *Bulletin of the Seismological Society of America* 90, 655–665. doi:10.1785/0119990021.
- Souriau, A., Chaljub, E., Cornou, C., Margerin, L., Calvet, M., Maury, J., Wathelet, M., Grimaud, F., Ponsolles, C., Pequegnat, C., Langlais, M., Guéguen, P., 2011. Multimethod characterization of the French-Pyrenean valley of bagnères-de-bigorre for seismic-hazard evaluation: Observations and models. *Bulletin of the Seismological Society of America* 101, 1912–1937. doi:10.1785/0120100293.

- Takahashi, T., Sato, H., Nishimura, T., Obara, K., 2007. Strong inhomogeneity beneath quaternary volcanoes revealed from the peak delay analysis of S-wave seismograms of microearthquakes in northeastern Japan. *Geophysical Journal International* 168, 90–99. doi:10.1111/j.1365-246X.2006.03197.x.
- Tertulliani, A., Cucci, L., 2014. New Insights on the Strongest Historical Earthquake in the Pollino Region (Southern Italy). *Seismological Research Letters* 85, 743–751. URL: <http://srl.geoscienceworld.org/cgi/doi/10.1785/0220130217>, doi:10.1785/0220130217.
- Totaro, C., Seeber, L., Waldhauser, F., Steckler, M., Gervasi, A., Guerra, I., Orecchio, B., Presti, D., 2015. An intense earthquake swarm in the southernmost apennines: Fault architecture from high-resolution hypocenters and focal mechanisms. *Bulletin of the Seismological Society of America* 105, 3121–3128. doi:10.1785/0120150074.
- Ugalde, A., Vargas, C., Pujades, L., Canas, J., 2002. Seismic coda attenuation after the Mw= 6.2 Armenia (Colombia) earthquake of 25 January 1999. *Journal of Geophysical Research: Solid Earth* 107. doi:10.1029/2001JB000197.
- Van Dijk, J.P., Bello, M., Brancaleoni, G.P., Cantarella, G., Costa, V., Frixia, A., Golfetto, F., Merlini, S., Riva, M., Torricelli, S., Toscano, C., Zerilli, A., 2000. A regional structural model for the northern sector of the Calabrian Arc (southern Italy). *Tectonophysics* 324, 267–320. doi:10.1016/S0040-1951(00)00139-6.

Xue, H., Ogawa, K., Shoji, T., 2009. Effect of welded mechanical heterogeneity on local stress and strain ahead of stationary and growing crack tips. *Nuclear Engineering and Design* 239, 628–640. URL: <http://www.sciencedirect.com/science/article/pii/S0029549309000314>, doi:<https://doi.org/10.1016/j.nucengdes.2008.12.024>.

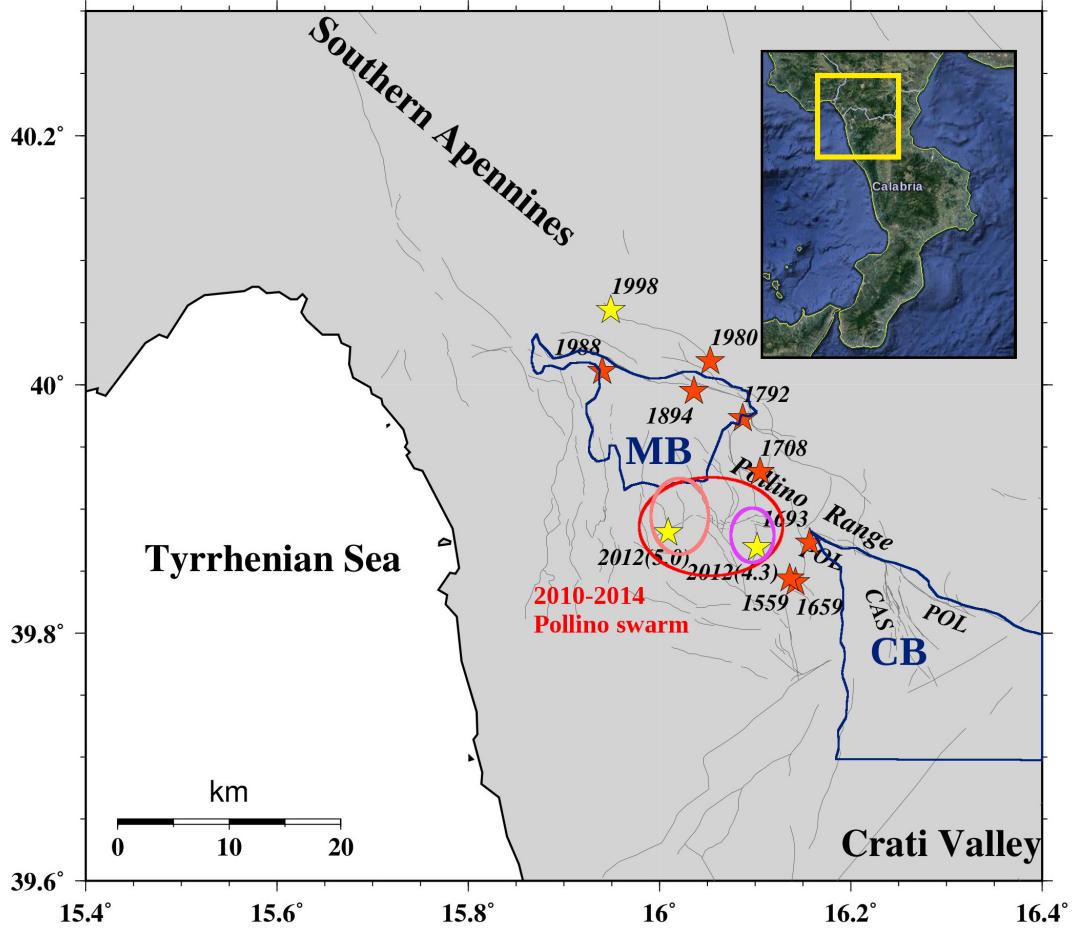


Figure 1: Map of the Pollino transition zone, located between the southern Apennines and the Crati Valley (yellow rectangle in the top right panel). Orange stars represent the presumed epicenters of historical earthquakes until 1988, yellow stars represent mainshocks occurred in the area in the last 20 years. MB and CB, bordered by blue lines, are the Mercure Basin and the castrovillari Basin, respectively. CAS and POL show the Castrovillari and Pollino Faults. The red ellipse surrounds the area of the 2010-2014 seismic swarm, which occurred in two slightly separated areas (smaller ellipses). Thin grey lines are the detailed faults from Brozzetti et al. (2017) in the Pollino area and from ITHACA catalogue for the outermost faults surrounding the Pollino area.

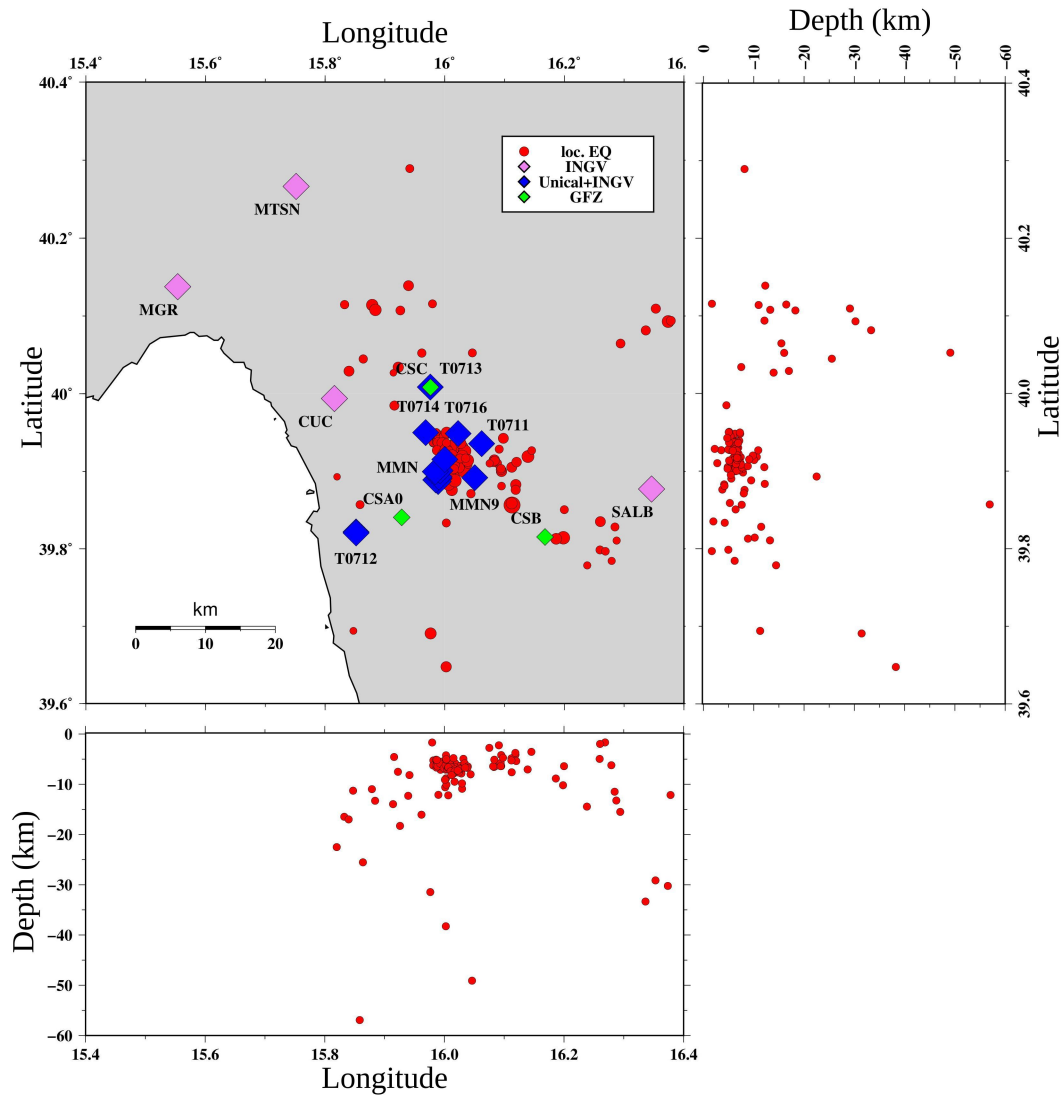


Figure 2: Map of the study area showing earthquakes used in this work (red circles) and seismic stations divided in three groups: permanent and temporary stations operated by the *Istituto Nazionale di Geofisica e Vulcanologia, INGV* (blue, Margheriti et al., 2013); temporary stations installed by GFZ (green, FDSN network code 4A, (Passarelli et al., 2012)); permanent and temporary stations operated by *Università della Calabria* (blue).

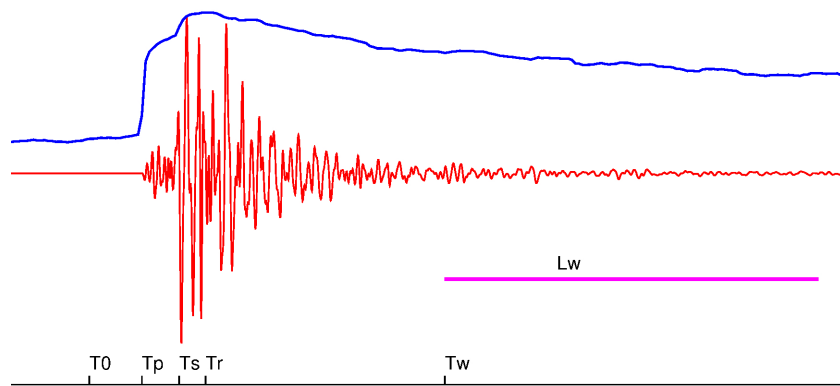


Figure 3: Example of a waveform (red line) used in this work and its envelope (blue line). T_p and T_s the P- and S-wave arrivals, T_r is the time at which the waveform reaches the maximum value, T_W is the beginning of the analysis window and L_W is its length. All these times are referenced to the origin time T_0 .

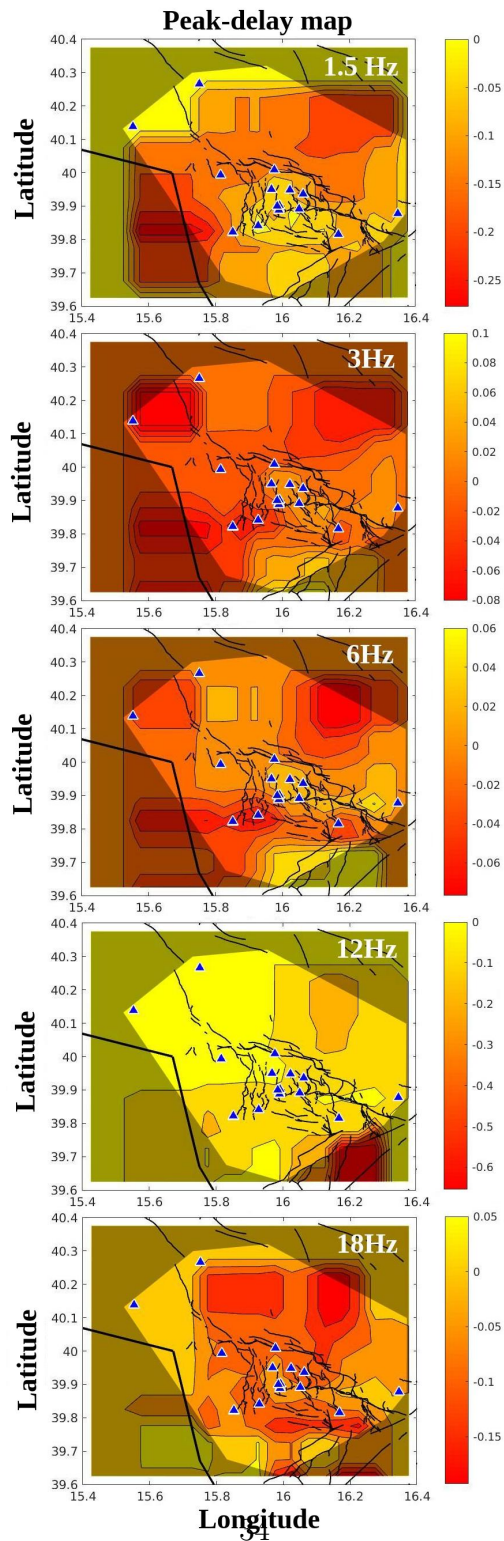


Figure 4: Peak-delay map. Central frequency is shown on the top-right for each panel, blue triangles represent seismic stations used in this work. Yellow colors represent high-scattering zones, red colors represent low-scattering zones.

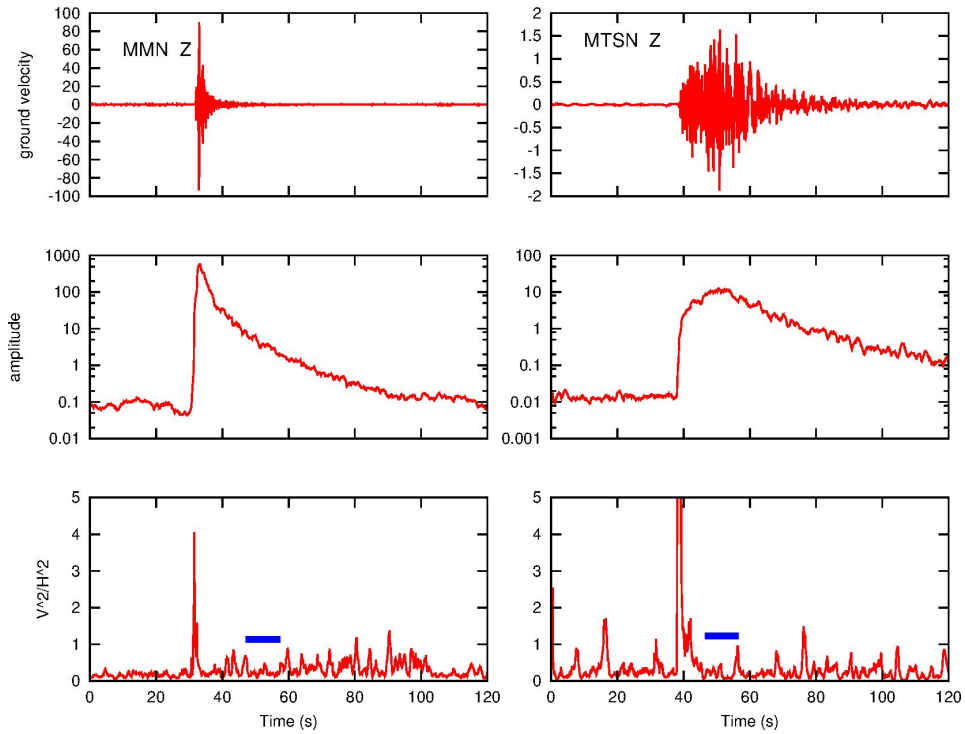


Figure 5: Equipartition of energy shown for one two earthquakes. The two earthquakes are characterized by small (4 km, on the left) and long (44 km, on the right) epicentral distance. From top to bottom: chosen seismograms; plot of the smoothed envelope and the mean noise amplitude; ratio between the kinetic energy of the vertical and horizontal components, V^2/H^2 . Blue segments represent the windows chosen to compute coda analysis.

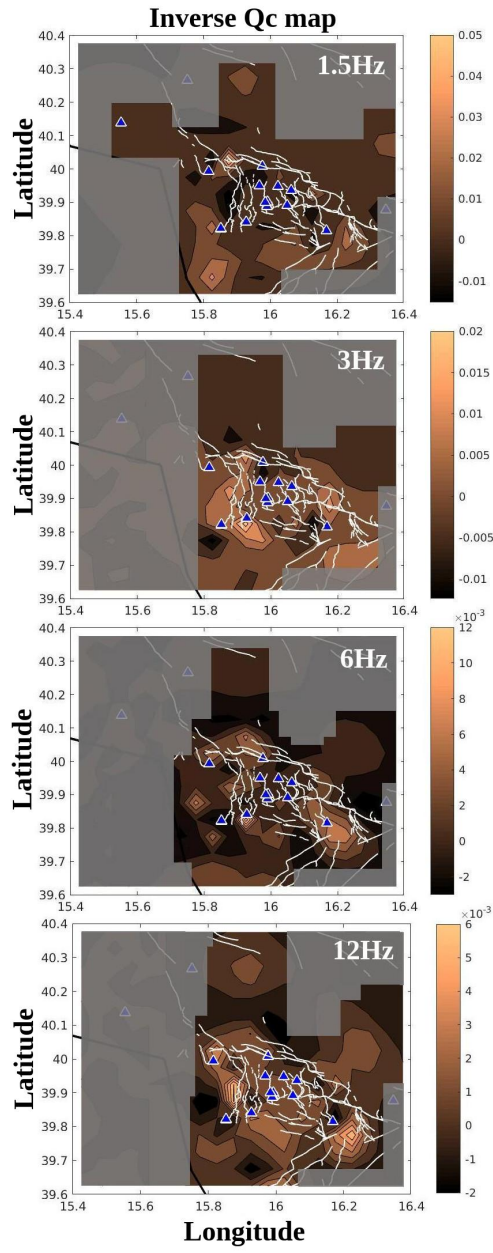


Figure 6: Inverse Q_c map. Central frequency is shown on the top-right for each panel, blue triangles represent seismic stations used in this work.

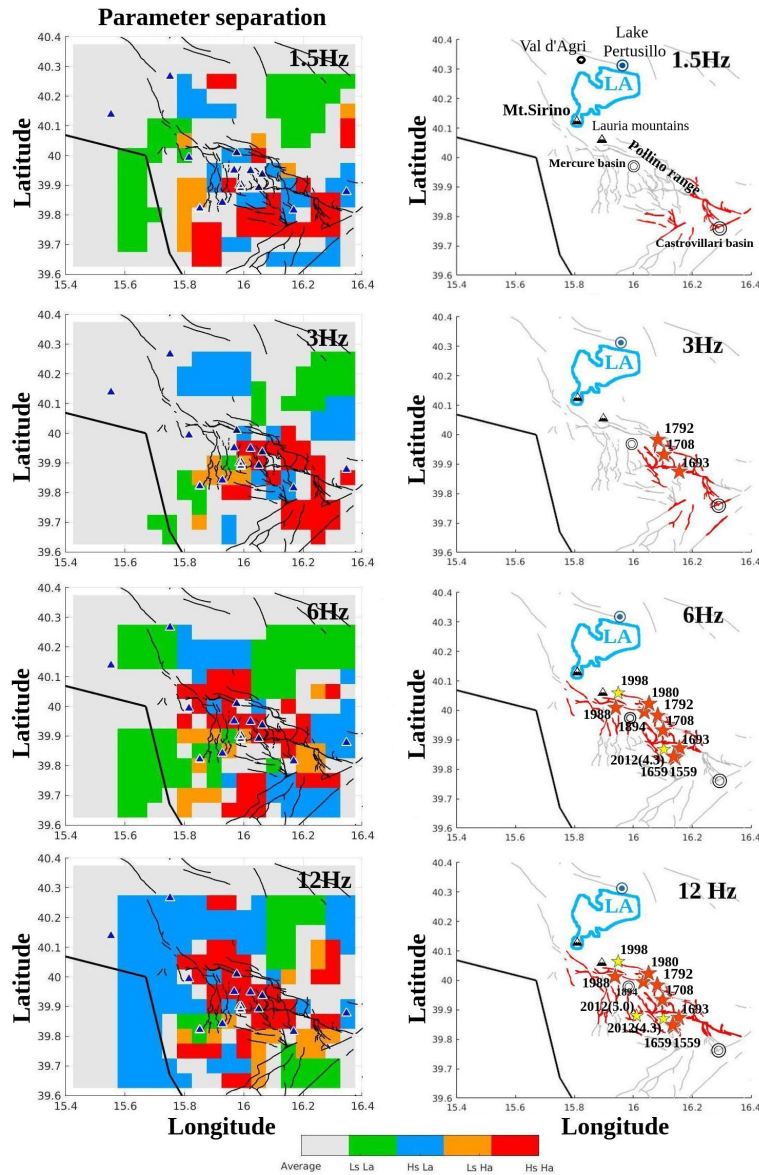


Figure 7: Attenuation and scattering results (left) and schematic interpretation of the stable and resolved patterns (right) obtained in 4 frequency ranges. Palette used: red - high scattering/high absorption, orange - low scattering/high absorption, cyan - high scattering/low absorption and green - low scattering/low absorption. Blue triangles show the seismic stations. The cyan pattern corresponding to the Lucanian Apennines (shortly named *LA*) extends from the Mount Sirino (SW) to the Lake Pertusillo (NE). Faults are coloured and stars (orange for earthquakes before 1998, yellow for more recent earthquakes) are displayed each time they are located in a red high scattering/high absorption block.